The nearly continuous improvement of discharge characteristics and edge stability with increasing lithium coatings in NSTX

R. Maingi[a], D.P. Boyle[b,c], J.M. Canik[a], S.M. Kaye[b], T.H. Osborne[e], C.H. Skinner[b], M.G. Bell[b], R.E. Bell[b], C.S. Chang[b], A. Diallo[b], S.P. Gerhardt[b], T.K. Gray[a], W. Guttenfelder[b], M.A. Jaworski[b], R. Kaita[b], H.W. Kugel[b], B.P. LeBlanc[b], J. Manickam[b], D.K. Mansfield[b], J.E. Menard[b], M. Ono[b], A. Pankin[e], M. Podesta[b], R. Raman[f], Y. Ren[b], A.L. Roquemore[b], S.A. Sabbagh[g], P.B. Snyder[d], V.A. Soukhanovskii[h]

[a]*Oak Ridge National Laboratory, Oak Ridge TN, 37831 USA*
[b]*Princeton Plasma Physics Laboratory, PO Box 451, Princeton, NJ, 08543 USA*
[c] *Princeton University, Princeton, NJ USA*
[d] *General Atomics, San Diego, CA USA*
[f] *Tech-X Corporation, Denver, CO, USA*
[g] *Univ. of Washington, Seattle, WA USA*
[g] *Columbia University, New York, NY, USA*
[h] *Lawrence Livermore National Laboratory, Livermore, CA, USA*

E-mail contact of main author: maingir@ornl.gov

Abstract. Lithium wall coatings have been shown to both improve energy confinement and eliminate ELMs in NSTX. Here, we present analysis of variable pre-discharge lithium evaporation from multiple experiments, for more insight into the pedestal expansion and ELM suppression physics. First, a nearly continuous improvement of a number of discharge characteristics, e.g. reduced recycling, ELM frequency, and edge electron transport, with increasing pre-discharge lithium evaporation has been identified. Profile and stability analysis clarified the mechanism responsible for ELM avoidance and the role of lithium: lithium coatings reduce recycling and core fueling; thus the density and its gradient near the separatrix are reduced. The temperature gradient near the separatrix is unaffected; hence the pressure gradient and bootstrap current near the separatrix are reduced, leading to stabilization of kink/peeling modes thought to be responsible for the NSTX ELMs. Thus, the enhanced edge stability with lithium coatings is correlated with the reduction of the pressure and its gradient near the separatrix. The key ingredient for ELM avoidance is control of the particle channel *independent* of the thermal channel at the edge: the density profile is continuously manipulated via the amount of lithium evaporation and resulting recycling control, leading to reduced neutral fueling. The surprising and beneficial facet of the NSTX data, however, is the continued growth of the edge transport barrier width in these circumstances, leading to 100% higher plasma pressure at the approximate top of the n_e profile barrier with high pre-discharge evaporation. Analysis shows enhanced edge transport; coupled with the heating power reduction to stay below the global beta limit, the pressure gradient and associated bootstrap current are maintained below the edge stability limit, thus avoiding ELMs. This allows the H-mode edge transport barrier to expand further and in such a way that peeling stability improves as a result of the inward shift of the bootstrap current.

1. Introduction

The understanding of regimes with 1) high pressure at the top of the H-mode pedestal, and 2) devoid of large ELMs is important for scenario optimization of ITER and future devices. In this paper we present analysis for a sequence of progressively increasing lithium coatings[1] in NSTX, demonstrating the nearly continuous improvement of the pedestal height and width

with increasing pre-discharge lithium evaporation[2]. In addition, we observed a nearly monotonic reduction in recycling, decrease in electron transport, and modification of the edge profiles and stability with increasing lithium[3]. These correlations ran contrary to initial expectations that the beneficial effects would saturate. The relevant scale length for deuterium retention is the implantation depth, which we estimated at 5-10 nm. On the other hand, the lithium evaporation in this experiment ranged from 30-500 nm thickness in the lower divertor, i.e. much larger than the implantation depth. It is becoming increasingly apparent that oxygen impurities are important in enhancing the deuterium retention in this mixed Li-C-D-O system[4, 5].

2. Effect of Variable Lithium Coatings on Discharge Characteristics

Elements of the lithium deposition scan have been described in a number of papers[2, 3, 6, 7], including a recent summary paper[8] that we follow for succinctness. A Type I ELMy H-mode scenario with boronized walls provided reference discharges. For completeness we note that the inter-ELM profile evolution[9] and turbulence[10] has been investigated in similar scenarios. To this ELMy scenario, increasing amounts of pre-discharge lithium were evaporated into the lower divertor. Helium glow discharge cleaning of 6.5 minute duration was used between all of the discharges, followed by lithium evaporation from two overhead evaporators. Figure 1 shows the lithium deposition between discharges during the sequence, as well as the cumulative deposition. The deposition rate was kept approximately constant for the first 9 discharges #129021-030, and was gradually increased in the subsequent discharges. Note that this sequence was the first use of lithium in that campaign, ensuring that the reference discharges were truly pre-lithium. The gas fueling, P_{NBI}, and boundary shape were held constant until the very end of the scan, when higher fueling and lower P_{NBI} were needed to avoid low density MHD and resistive wall modes. The dependence of various discharge parameters as a function of pre-discharge lithium deposition is shown in Figure 2. Panels (a) and (b) show that the divertor D_α and midplane neutral pressure gradually decreased with

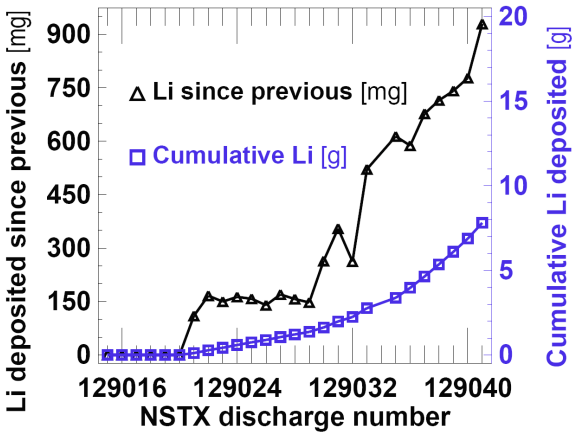

Figure 1: Lithium deposition during the systematic experiment: pre-discharge lithium evaporation (triangles), and cumulative lithium coating (squares).

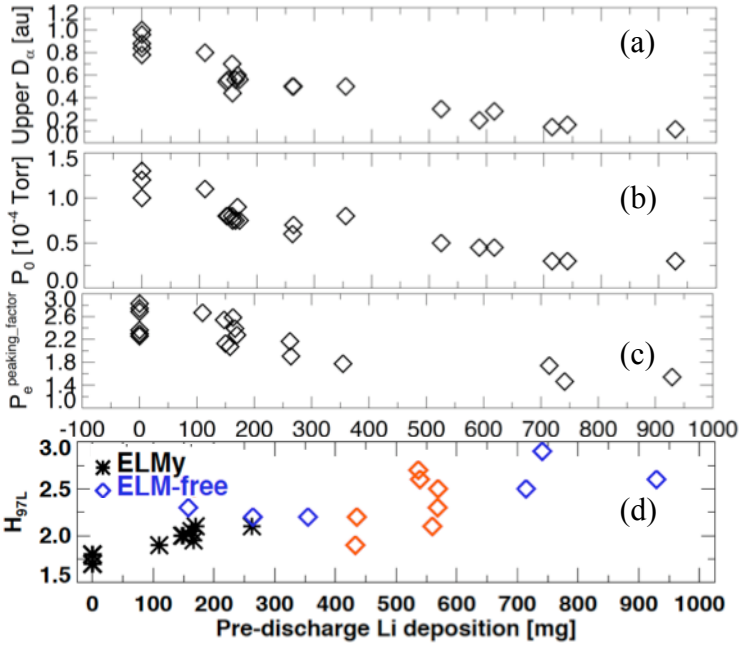

Figure 2: Evolution of discharge quantities as a function of pre-discharge lithium evaporation: (a) divertor D_α, (b) midplane neutral pressure, P_0, (c) electron pressure profile peaking factor, and (d) energy confinement relative to ITER97-L scaling at time of peak β_N. The ELMy discharges and ELMy-free discharges are separated by symbol type in panel (d). Also data from additional ELM-free discharges from other experiments are displayed by the orange symbols.

increasing lithium coatings. Panel (c) shows that the electron pressure (P_e) profile peaking factor decreased nearly monotonically with increasing lithium, while panel (d) shows that the confinement enhancement factor relative to the ITER97 L-mode scaling increased gradually during the coating scan. Note that data from several additional ELM-free discharges at intermediate deposition rates is also shown in panel (d)[11]. In addition, the ELM frequency also decreased during the coating scan, with robustly ELM-free discharges obtained when the evaporation exceeded ~ 300mg.

The temporal evolution of the divertor D_α for each discharge in the sequence is shown in Figure 3. The external gas fueling was held constant until #129036, and then it was increased for the subsequent discharges. The P_{NBI} was held constant at 4 MW until #129033, after which it was reduced in steps to avoid the locked modes. The effects of lithium are apparent in the second lithiated discharge #129022, in that the ELM frequency was visibly reduced. ELM-free periods of increasing duration are evident in and after #129024, but the progression to fully ELM-free operation was not monotonic. Specifically discharges that 'failed', e.g. #129026, which had no auxiliary heating, or discharges with particularly virulent MHD modes followed by long L-mode phases, e.g. #129028 and the end of

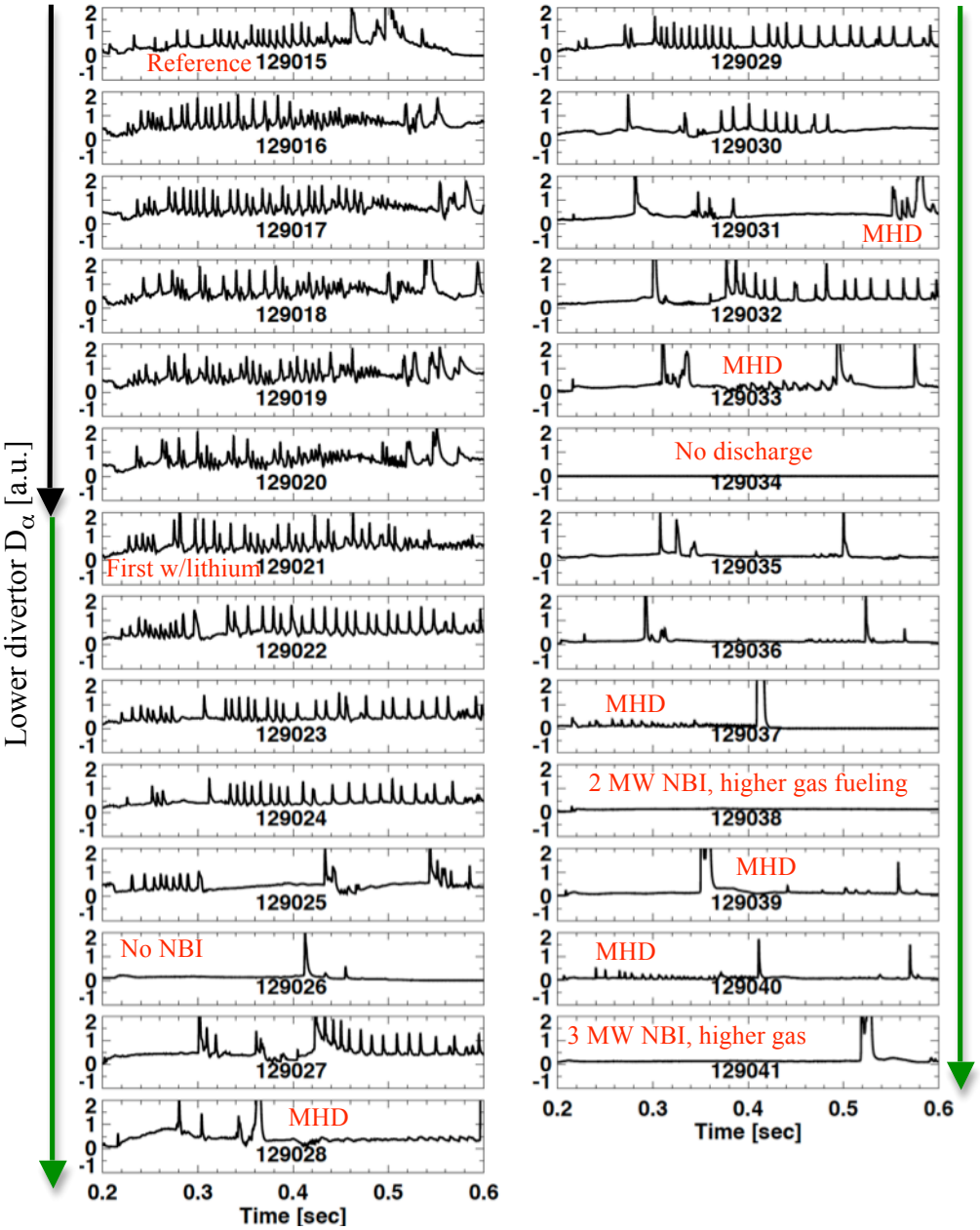

Figure 3: Evolution of lower divertor D_α emission during discharge sequence, showing the gradual effect of increasing lithium evaporation on ELM activity. The black vertical arrow indicates reference, non-lithiated discharges (#129015-020), and the green arrows show lithiated discharges.

#129031, were followed by discharges with higher ELM frequency and higher recycling. The discharges #129033 and #129035 - #129037 did not achieve sustained H-mode phases, as the combination of reduced heating power and increased external fueling was not optimized until #129038. Discharges #129039 and #129041 both disrupted at 0.35sec and 0.515 sec respectively, as a result of higher β_N from an increased of P_{NBI} to 3 MW. In addition, #129041 had modestly higher external gas fueling than #129038 and #129039.

3. Effect of Variable Lithium Coatings on Confinement, Transport, and ELM stability

Figure 4 shows the results of the TRANSP analysis of the discharge sequence[8]. Panel (a) shows that the plasma total and thermal stored energy increased with lithium deposition at constant P_{NBI}. Note that the last three discharges had reduced P_{NBI}. Panel (a) shows that both the total and electron τ_E increased with increasing lithium deposition; indeed, the electron τ_E increased more rapidly than the global τ_E. Panel (b) shows that the edge electron thermal diffusivity, χ_e, at r/a=0.7 decreased strongly with increasing lithium deposition; in contrast the ion thermal diffusivity, χ_i, actually increased modestly. The ion momentum diffusivity, χ_ϕ, was insensitive to the amount of lithium deposition, except for two of the last three discharges with the highest evaporation rate and the lowest torque input. On the other hand, the core χ_e, χ_i, and χ_ϕ at r/a=0.35 were insensitive to or weakly increasing with the pre-discharge lithium deposition[8]. These results agree with analysis[12] of a broader dataset, which included a couple of the discharges from this scan, and they also agree with the overall trend of decreasing electron transport at reduced collsionality[13]. In addition, dedicated modelling of the profiles with the SOLPS suite of codes showed that both the cross-field particle diffusivity and electron thermal diffusivity dropped nearly continuously with increasing lithium deposition in the region from $0.8 < \psi_N < 0.94$, i.e. the drop in the transport extended all the way out to near the separatrix[7].

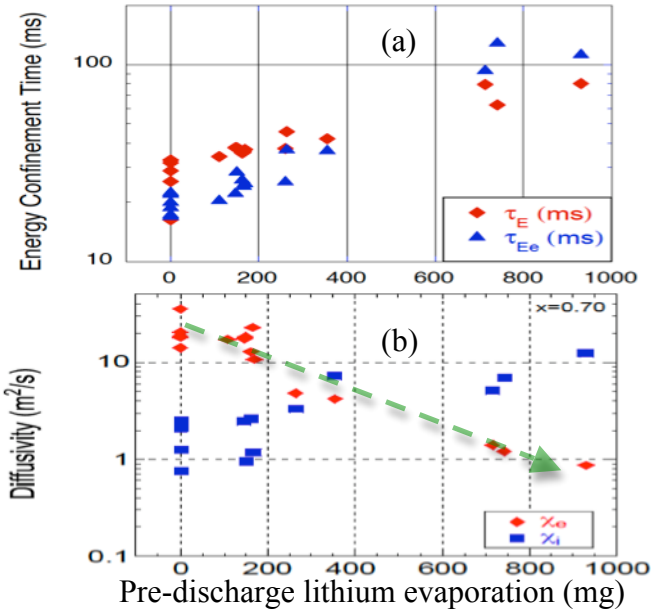

Figure 4: Results of core transport analysis as a function of pre-discharge lithium evaporation: (a) total and electron τ_E, and (b) cross-field diffusivities χ_i, χ_e, and χ_ϕ at r/a = 0.7. The dashed arrow in panel (b) is intended to highlight the trend.

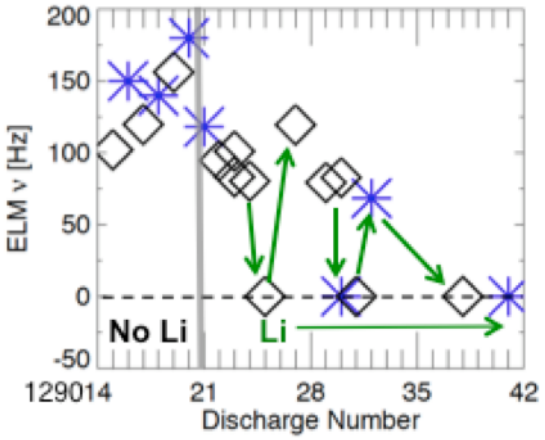

Figure 5: Average ELM frequency during the lithium evaporation scan; discharges with both ELMy and ELM-free periods of duration > 100ms are shown with multiple data points.

Fig. 5 shows that the measured ELM frequency during discharges from this sequence decreased with increasing discharge number, i.e. increasing lithium deposition. As evident in Figure 3, the transition to ELM-free operation was not quite monotonic, however, in that

several discharges with substantial ELM-free periods were followed by ELMy discharges. The data points in black in Figure 5 had edge profiles that were analyzed with a standard ELM-synchronization method[14], whereas the data points in blue were unsuitable for profile analysis, but were included for more insight into the ELM frequency trend. There are several discharges with more than one data point per discharge in Figure 5; in those cases, the edge profiles were analyzed in non-overlapping time windows of duration ~ 0.1 sec. This was necessary because the discharges had both an ELMy and an ELM-free phase, or long ELM-free phases with evolving density.

The n_e, T_e, and P_e composite profiles were fitted[3] with a 'standard' modified hyperbolic tangent ("mtanh") function[15], which included both a tanh component and a linear component. The n_e and P_e profile widths were both shown to order the ELMy and ELM-free data, mostly as a threshold criterion[2, 3]. The T_e profile width was immediately ruled out as an ordering parameter. Since the lithium mainly changes the recycling and the edge fueling, these trends support the conclusion that the density profile change is central to the ELM suppression[3, 16]. In addition to the profile widths, the profile fitting yields the pedestal top value and its location, the peak gradient and its location, and the pedestal bottom value and its location. A comprehensive analysis of the correlation between ELM frequency and the other parameters from the mtanh fits showed that ELMy and ELM-free discharges were also organized by the location of the peak n_e and P_e gradients[3, 8], i.e. the symmetry point of the tanh function. This is unsurprising, because as the characteristic width of a profile grows, the location of its peak gradient shifts also. It is relevant, however, because the location of the symmetry point coincides with the location of the peak bootstrap and local parallel current density in the kinetic equilibria; increasing the separation between this current and the separatrix reduces the drive for kink/peeling modes.

As shown in Figure 5, the transition to ELM-free operation was not monotonic with discharge number. The edge stability of this sequence was analyzed[3] with the ELITE code[17]; Figure 6 shows the results for four of these discharges, including one portion where an ELM-free discharge (#129031, panel (b)) was followed by an ELMy one (#129032, panel (c)). The panels display contours of the growth rate γ_{lin} normalized by the diamagnetic drift frequency ($\omega^*/2$), and the transition between blue to red represents the nominal instability threshold where ELMs are typically observed in NSTX. The two ELMy discharges (panels (a), (c)) lie close to the kink/peeling instability boundary, whereas the ELM-free discharges (panels (b), (d)) have larger margin to the instability threshold.

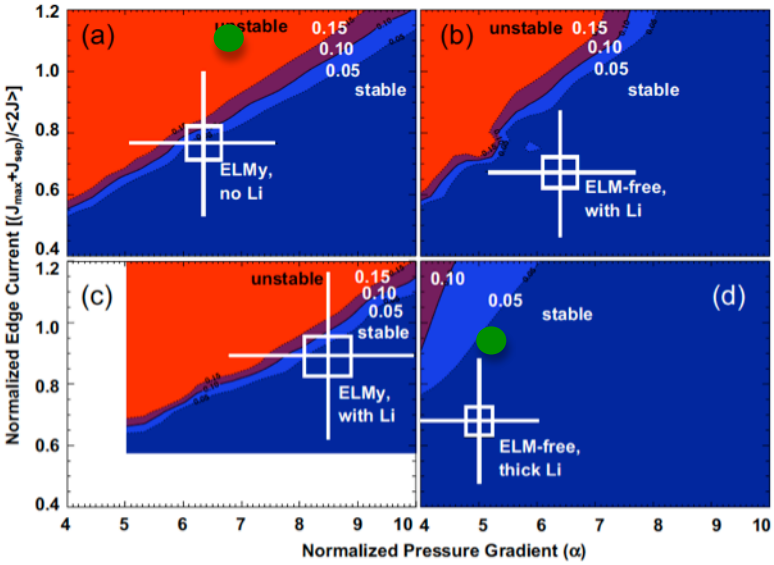

Figure 6: edge stability with the ELITE code for (a) 129019, (b) 129031, (c) 129032, and (d) 129038 (see Fig. 3). The green circles represent the new values of α and J from the XGC code bootstrap calculation.

Note that the computed growth rates at the time of ELM onset in NSTX are lower than typically encountered at higher aspect ratio R/a[18] when using the standard Sauter formulation for bootstrap current[20]. Specifically the $\gamma_{lin}/(\omega^*/2)$ is typically ~

0.1 at ELM onset in NSTX, as compared to 0.5-1 at higher R/a. A recent revision to the bootstrap current calculation with the XGC code[19] has shown that the bootstrap current using the Sauter formula[20] is underestimated by up to 33% in intermediate collisionality at low R/a. Using the XGC formulation of the bootstrap current, the experimental values of normalized pressure gradient and current were re-computed; these are represented by the solid green dots in panels (a) and (d). This revision increases the experimental linear growth rate substantially, up to the 50% of the value of (ω*/2), in line with the growth rates observed at the ELM onset at higher R/a[21]. The recalculation of the normalized pressure and current for panels (b) and (c) is in progress, and will be presented in future publications. One final note: the 'unstable' labels in Figure 6 were left unchanged as they appeared in previous studies [3, 16], but will be adjusted in future publications to line up with the contour that corresponds to $\gamma_{lin}/(\omega^*/2)=1$.

4. Summary, Discussion and Conclusions

Recent interpretive edge transport analysis[7] with SOLPS and stability analysis[3] with ELITE has clarified the mechanism responsible for ELM avoidance: lithium coatings reduce recycling and core fueling; thus the density and its gradient near the separatrix are reduced. The T_e gradient near the separatrix (from $0.95<\psi_N<1$) is unaffected; hence the pressure gradient P′ and bootstrap current near the separatrix are reduced, leading to stabilization of kink/peeling modes thought to be responsible for the NSTX ELMs. The surprising facet of these data, however, is the growth of the edge transport barrier width, leading to substantially higher plasma pressure at $\psi_N \sim 0.8$, the approximate top of the n_e profile barrier with high pre-discharge evaporation. Figure 7 illustrates the dependence of the n_e, T_e, P_e and total pressure (P_{e+i}) values at two different radial locations, $\psi_N=0.95$ and $\psi_N=0.8$, as a function of pre-discharge lithium. Panel 7a shows that the n_e at $\psi_N=0.95$ decreased with increasing lithium (mostly due to the reduction of the recycling source), but the n_e deeper into the plasma at $\psi_N=0.8$ was relatively unchanged. In contrast, the T_e values at $\psi_N=0.95$ were unchanged, but increased substantially at $\psi_N=0.8$ in panel 7b. The P_e and P_{e+i} values at $\psi_N=0.95$ decreased with the n_e, whereas they increased substantially at $\psi_N=0.8$, following the T_e. Panels 7c and 7d show a P_e (P_{e+i}) threshold of 1 kPa (2 kPa) corresponds to the transition from ELMy to ELM-free operation.

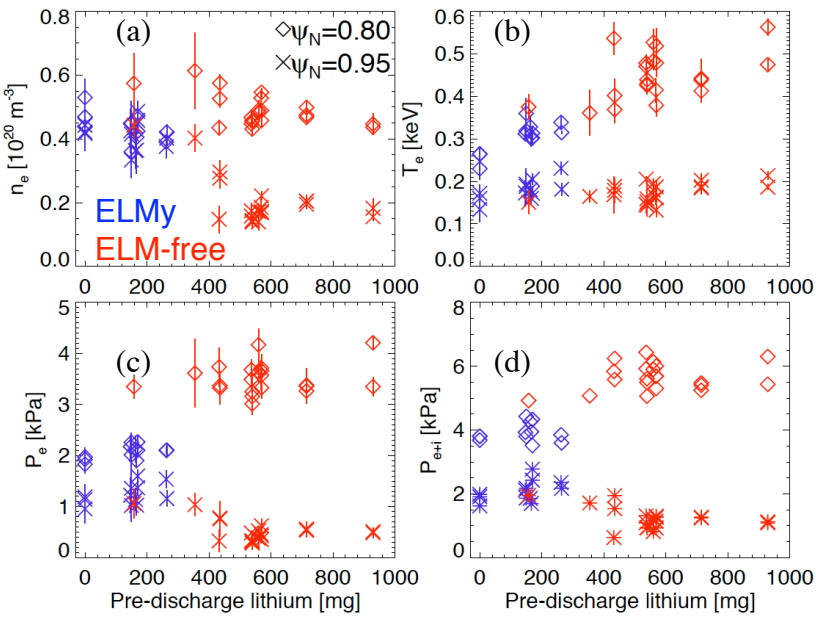

Figure 7: Near-separatrix ($\psi_N=0.95$) and radially inward ($\psi_N=0.8$) values of (a) n_e, (b) T_e, (c) P_e, and (d) P_{e+i} as a function of pre-discharge lithium evaporation. The red and blue data are from time slices without and with ELMs, respectively.

Neglecting variations in the separatrix pressure (which is constrained by open field line physics and much smaller than the pedestal pressure in any event), the trend of the pressure at $\psi_N=0.95$ is nearly identical to that of the peak pressure gradient between $0.95 < \psi_N < 1$. Thus, the enhanced edge stability with lithium coatings is correlated with the reduction of the pressure and its gradient from $0.95<\psi_N<1$. In qualitative agreement with peeling-ballooning

physics, the pedestal width and pedestal top pressures increase substantially with the reduction of P′.

Figure 8 summarizes these results by displaying schematically the steps by wall lithium wall coatings lead to ELM suppression. For a complete discussion, we break the profile effects into two spatial regions: the near-separatrix region representing the pedestal extent in reference ELMy discharges from $0.95 < \psi_N < 1$, and the spatial region over which the n_e gradient is extended with lithium coatings, i.e. from $0.8 < \psi_N < 0.95$.

In the outermost region $0.95 < \psi_N < 1$:

1) Lithium reduces recycling, due to its affinity for atomic hydrogenic species
2) The core fueling from divertor recycling sources is reduced, reducing the edge n_e gradient
3) The T_e gradient is clamped, however, and the reason for this is being investigated[22]
4) The P_e gradient is reduced, in proportion to the n_e gradient.
5) The P_i gradient is relatively unchanged, such that the overall P' is reduced, just as P_e gradient
6) The parallel current is reduced because of the reduction of the bootstrap current from the reduced pressure gradient; this moves the experimental data point away from the instability threshold

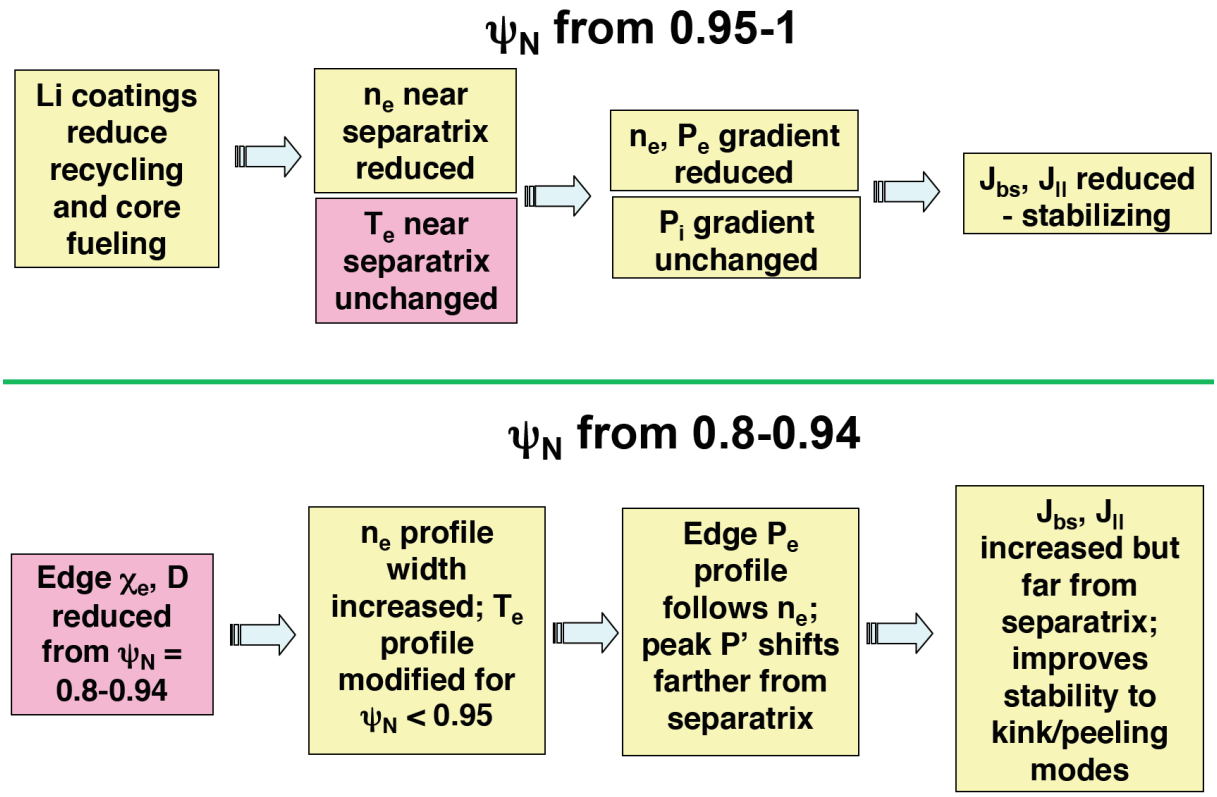

Figure 8: Flowchart showing how lithium coatings lead to the change of edge profiles and suppression of ELMs. The yellow boxes represent connections that are (at least) semi-quantitatively understood; the cause for the invariance of the near-separatrix T_e gradient and the reduction in transport (pink boxes) is still being investigated.

In the inner region from $0.8 < \psi_N < 0.95$:

1) The edge n_e gradient is extended inward with lithium coatings into $\psi_N \sim 0.8$; the edge cross-field particle diffusivity is inferred to decrease[7]
2) The edge thermal transport is reduced, possibly due to stabilization of micro-tearing modes[22] due to the increase of the n_e gradient[23]; the edge T_e rises correspondingly
3) The edge pressure profile follows both the n_e and T_e profiles, leading to an increased P' far from the separatrix
4) The bootstrap current and parallel current increase; however, this is stabilizing to kink/peeling modes because of the distance from the separatrix, i.e. the instability boundary moves to higher current density (reason under investigation)

The key ingredient for ELM avoidance is control of the particle channel independent of the thermal channel from $0.95 < \psi_N < 1$. The density profile is continuously manipulated via the amount of lithium evaporation, via recycling control, leading to reduced neutral fueling.

This research was sponsored by the U.S. Dept. of Energy under contracts DE-AC05-00OR22725, DE-AC02-09CH11466, DE-FC02-04ER54698, DE-AC52-07NA27344, DE-FG03-99ER54527 and DE-FG02-99ER54524. We gratefully acknowledge the contribution of the NSTX technical and operations staff.

References:

[1] Kugel H. W., *et al. J. Nucl. Mater.* **415,** S400(2011).
[2] Maingi R., *et al. Phys. Rev. Lett.* **107,** 145004(2011).
[3] Boyle D. P., *et al. Plasma Phys. Control. Fusion* **53,** 105011(2011).
[4] Taylor C. N., *et al. J. Nucl. Mater.* **415,** S777(2011).
[5] Allain J. P., *et al. Phys. Plasmas* **19,** 056126(2012).
[6] Mansfield D. K., *et al. J. Nucl. Mater.* **390-391,** 764(2009).
[7] Canik J. M., *et al. Phys. Plasmas* **18,** 056118(2011).
[8] Maingi R., *et al. Nucl. Fusion* **52,** 083001(2012).
[9] Diallo A., *et al. Nucl. Fusion* **51,** 103031(2011).
[10] Diallo A., *et al. Proc. 24th IAEA Fusion Energy Conf., San Diego, CA, Oct. 8-13, 2012* EX/P4_4(2012).
[11] Boyle D., *et al. J. Nucl. Mater.* submitted(2012).
[12] Ding S., *et al. Plasma Phys. Control. Fusion* **52,** 015001(2010).
[13] Kaye S. M., *et al. Proc. 24th IAEA Fusion Energy Conf., San Diego, CA, Oct. 8-13, 2012* paper EX/7_1(2012).
[14] Osborne T. H., *et al. J. Phys.: Conf. Series* **123,** 012014(2008).
[15] Groebner R. J., *et al. Phys. Plasmas* **5,** 1800(1998).
[16] Maingi R., *et al. Phys. Rev. Lett.* **103,** 075001(2009).
[17] Snyder P. B., *et al. Phys. Plasmas* **9,** 2037(2002).
[18] Snyder P. B., *et al. Plasma Phys. Control. Fusion* **46,** A131(2004).
[19] Koh S., *et al. Phys. Plasmas* **19,** 072505(2012).
[20] Sauter O., *et al. Phys. Plasmas* **6,** 2834(1999).
[21] Chang C. S., *et al. Proc. 24th IAEA Fusion Energy Conf., San Diego, CA, Oct. 8-13, 2012* TH/P4_12(2012).
[22] Canik J. M., *et al. Proc. 24th IAEA Fusion Energy Conf., San Diego, CA, Oct. 8-13, 2012* paper EX/P7_16(2012).
[23] Guttenfelder W., *et al. Phys. Rev. Lett.* **106,** 155004(2011).